

Analysis and Experimental Validation of a Low-Complexity Enhanced Orientation-Based Controller for Tethered Energy-Harvesting Systems

Jacob B. Fine^{ID}, Peter Newell, Kavin Govindarajan^{ID}, Carson McGuire^{ID}, Paul Paris, Gabriel Matthias, Mary Maceda, Jonathan Baxter, Kenneth Granlund^{ID}, Matthew Bryant^{ID}, and Chris Vermillion^{ID}

Abstract—In this work, a methodology for controlling the flight of an underwater energy-harvesting kite, termed enhanced orientation-based control, is presented. This control technique is shown to perform comparably to more complex, hierarchical path-following control approaches that rely upon expensive and unreliable localization sensors while performing significantly better than simple orientation-based controllers that possess a comparable degree of complexity. The periodic closed-loop stability of a kite utilizing the proposed controller is validated in a low-order simulation framework. From there, the performance of the proposed controller is benchmarked against established control techniques via a medium-fidelity simulation environment. Finally, the efficacy of the proposed controller design is demonstrated experimentally based on two testing results on a scaled prototype kite.

Index Terms—Autonomous underwater vehicles, energy harvesting, nonlinear control, power generation, stability analysis.

NOMENCLATURE

Variable	Description
θ	Elevation angle.
λ	Azimuth angle.
$\dot{\theta}$	Elevation rate.
$\dot{\lambda}$	Azimuth rate.
$r_{k/o,x}$	Ground-frame x -position.
$r_{k/o,y}$	Ground-frame y -position.
$r_{k/o,z}$	Ground-frame z -position.
ϕ	Roll angle.

Received 4 November 2024; revised 20 February 2025; accepted 25 March 2025. This work was supported in part by DARPA and in part by North Carolina Coastal Studies Institute's Renewable Ocean Energy Program. This work is approved for public release: distribution is unlimited. Recommended by Associate Editor K. Worthmann. (*Corresponding author: Jacob B. Fine*)

Jacob B. Fine is with the Department of Mechanical Engineering, University of Michigan, Ann Arbor, MI 48109 USA (e-mail: jbfine@umich.edu).

Peter Newell, Kavin Govindarajan, Carson McGuire, Mary Macea, Jonathan Baxter, Kenneth Granlund, and Matthew Bryant are with the Department of Mechanical and Aerospace Engineering, North Carolina State University, Raleigh, NC 27695 USA (e-mail: jpnewel2@ncsu.edu; kmgovind@ncsu.edu; cmmcuire@ncsu.edu; memaceda@ncsu.edu; jwbaxter@ncsu.edu; kgranlu@ncsu.edu; mbryant@ncsu.edu).

Paul Paris and Gabriel Matthias are with North Carolina Coastal Studies Institute, Wanchese, NC 27981 USA (e-mail: Parisp15@ecu.edu; gabrielmatthias@yahoo.com).

Chris Vermillion is with the Department of Mechanical Engineering, University of Michigan, Ann Arbor, MI 48109 USA, also with Altaeros Energies Inc., Fremont, NH 03044 USA, and also with Windlift Inc., Durham, NC 27713 USA (e-mail: cvermill@umich.edu).

Digital Object Identifier 10.1109/TCST.2025.3558870

ζ	Pitch angle.
ψ	Yaw angle.
u_{kite}	Body-frame velocity x -component.
v_{kite}	Body-frame velocity y -component.
w_{kite}	Body-frame velocity z -component.
p	Rotational rate about the kite's body-frame x -axis.
q	Rotational rate about the kite's body-frame y -axis.
r	Rotational rate about the kite's body-frame z -axis.

I. INTRODUCTION

OVER the past few decades, there has been a sizable uptake in the adoption of marine hydrokinetic (MHK) systems. These devices offer sustainable, cost-effective methods for harnessing tidal and ocean current energy. These energy sources have immense potential, with an estimated 334 TWh per year of tidal energy [1] and 163 TWh per year of ocean current energy [2] available off the coast of the United States alone. To tap into this abundant resource, the development of MHK systems that can provide utility-scale power as well as power to remote locations is underway [3]. Beyond their applications at grid-scale, MHK systems also play a crucial role in powering the “blue economy,” which encompasses various offshore devices such as marine buoys, autonomous vehicles, and navigational aids [4].

However, a significant challenge in harvesting tidal and ocean current energy is that the regions with the highest energy density are often not economically viable for deploying MHK systems. This challenge arises due to factors like the considerable depth of seafloor, as observed in the U.S. Gulf Stream [5], or the distance from energy consumers. A similar situation is encountered in wind energy, where the peak energy density exists at altitudes ranging from 500 to 1000 m [6]. To address this challenge, one solution is to use energy-harvesting kites, which execute high-speed flight patterns that can deliver significantly more power for a given mass and flow speed than stationary turbines. Companies like Windlift [7] (airborne), Kitepower [8] (airborne), and Minesto [9] (underwater) have developed such systems. These kites, whether airborne or underwater, follow figure-eight (or elliptical), cross-current patterns perpendicular to the prevailing flow, as described in

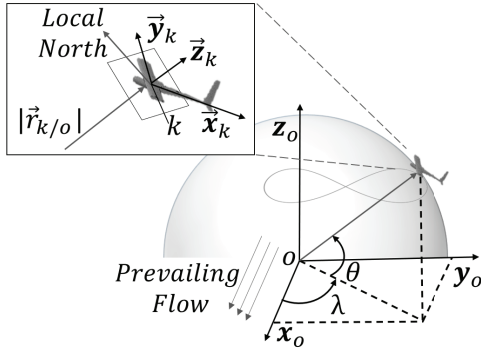


Fig. 1. Key variables in the dynamic model from [22] (used with permission). The k and o frame orthonormal coordinate systems, elevation angle θ , azimuth angle λ , kite velocity \vec{v}_k , as well as the distance from the o frame to the k frame $|r_{k/o}|$ are shown.

[10]. This work will focus on figure-eight flight, which carries the advantage that it does not introduce continual twists into the tether and, therefore, avoids the need to introduce a slip ring at the tether/kite interface. Similar to how a sailboat can outpace the wind by positioning its sail at a desirable angle of attack relative to the wind, kites use a high lift-to-drag wing to achieve speeds 5–10 times higher than the prevailing flow speed, thereby facilitating cost-effective energy capture even in low-flow environments. The energy from these kite systems can be harnessed using either onboard turbines (referred to as “fly-gen” operation) or through cyclic spooling of a ground-mounted winch system (referred to as “ground-gen” operation). The present research focuses specifically on the “fly-gen” operation, where electricity is generated by onboard turbines and transmitted down the tether, as depicted in Fig. 1.

In the realm of energy-harvesting kites, several aspects of the control system significantly influence the average power output over a cycle (the lap-averaged power). These attributes include the width of the figure-eight pattern, its height, and the mean elevation angle (the angle formed between the straight line connecting the kite and the tether attachment point and the horizontal plane). Consequently, there has been a proliferation of studies over the past two decades that delve into optimal control strategies and learning control mechanisms. For instance, works such as [11], [12], [13], and [14] have applied optimal control strategies to shape the figure-eight pattern of the kite’s trajectory. Meanwhile, our group’s previous work in [15] and [16] concentrated on optimizing the elevation angle profile while taking flow turbulence into account.

Despite successful efforts to enhance power output through control, the majority of previous works utilize control strategies that require a measurement of the kite’s position, closing the loop on a desired flight path (*path-following control*). While this control strategy has proved extremely successful experimentally in airborne systems, such as [7], measuring the position of an airborne kite is made relatively easy through the use of GPS. Conversely, knowing the precise position of a fast-moving underwater kite in real time is extremely challenging, given that GPS signals cannot propagate underwater. High-accuracy measurements of underwater position require

expensive acoustic equipment such as an ultrashort baseline (USBL) tracking system. These devices are both costly and suffer from reliability issues in the presence of turbulent flows. Furthermore, the majority of path-following control strategies rely upon complex, multitiered hierarchical controllers [14], [17]. When compared with a centralized controller, the advantage of a hierarchical controller in this application is that the presence of multiple nested feedback loops renders the closed-loop system less sensitive to uncertainty in the dynamics of the complex, highly nonlinear system. This robustness to model uncertainty comes at a high development and calibration cost, however, owing to the need to tune several layers of the controller and a multitude of parameters. These issues necessitate the development of low-complexity control strategies for underwater kite systems that: 1) do not rely on direct position measurements for closed-loop control and 2) minimize the complexity of the control algorithm.

To avoid the complexity of path-following control, simpler control strategies that rely upon orientation measurements (*orientation-based control strategies*), conventionally via an inertial measurement unit (IMU), have been developed and implemented in our group’s prior work [18], [19]. These strategies involve the tracking of periodic roll-and-yaw set-point trajectories, enabling figure-eight flight. While reliable, orientation-based strategies are less effective than control strategies that close the loop on position directly [19]. A large reason for this is the lack of control over the kite’s elevation angle, θ . As described in [10], the power a kite system can generate is proportional to $\cos^3 \theta$. At first glance, it may seem desirable to simply target as low of an elevation angle as possible. However, this approach is suboptimal in any practical shear profile, where the depths closest to the seabed are associated with the lowest flow speeds. In practice, there is a time-varying optimal elevation angle for the kite to operate at (as explored in [20]). Because orientation-based control alone does not close the loop on elevation angle, power generation is significantly reduced when compared to path-following control strategies that do close the loop on elevation angle.

The present paper describes a novel control architecture, termed *enhanced orientation-based control*, wherein the roll angle setpoint trajectory is adjusted for a figure-eight to drive the kite to a desired elevation angle. This control strategy utilizes a depth measurement (pressure-based sensors capable of rapidly and precisely measuring depth alone are inexpensive and reliable), in combination with the measured tether length, to estimate the value of θ . This enables closed-loop control over the kite’s elevation angle. This strategy will be shown to achieve similar performance to a path-following control strategy and outperform an orientation-based control strategy, while only relying upon measurements of orientation and depth. We will present an orbital stability analysis of the closed-loop system under this control technique, using a low-order dynamic model. In previous work ([21]), a similar low-order model was used to analyze the orbital stability of an underwater kite using a path-following control strategy. The stability properties identified in this analysis were subsequently validated via stroboscopic intersection analysis using a higher-fidelity dynamic model. While thorough,

this previous work exclusively analyzed the orbital stability properties of a single kite system using a path-following controller. The present work uses a similar analysis technique to validate the periodic stability properties of multiple kite systems using both an orientation-based control strategy and the proposed enhanced orientation-based control strategy (both of which differ substantially from the control approach used in [21]).

Following this orbital stability analysis, we will then present simulations that use a medium-fidelity dynamic model to compare the efficacy of the proposed control strategy to existing control strategies (path-following control and orientation-based control). Finally, experimental results benchmarking the proposed control strategy with an orientation-based control architecture using a prototype ocean energy harvesting kite will be presented. In this work, two kite models are examined: 1) an open-source model described in our group's prior work ([14]) and 2) a proprietary model used for experimental studies. The parameters of the open-source kite design are included in this work for reproducibility, and associated analysis and simulation results are provided for this model throughout the article. Given that the design of the second kite model is proprietary, the parameters cannot be disclosed, and the associated simulation and experimental results have been nondimensionalized.

In summary, the contributions of this effort are as follows.

- 1) We present a control strategy for simultaneous tracking of roll, yaw, and elevation angle setpoints.
- 2) We validate the orbital stability of a closed-loop system utilizing the proposed control technique through a Floquet analysis using a low-order dynamic model.
- 3) We present medium-fidelity dynamic simulation results benchmarking the proposed architecture against existing control strategies.
- 4) We present experimental results benchmarking the efficacy of the proposed control strategy to an orientation-based control strategy.

The remainder of this article is organized as follows. In Section II, the dynamic models used in this work are introduced. Following this, the details of the developed controller design, as well as existing controller designs, are presented in Section III. Next, the orbital stability of the closed-loop system utilizing the proposed controller is demonstrated in Section IV. After demonstrating orbital stability, medium-fidelity dynamic simulations of the three control strategies are presented in Section V. Lastly, an experimental validation of the proposed control strategy benchmarked against an orientation-based control strategy is shown in Section VI.

II. PLANT MODEL

A. Low-Order Dynamic Model

A low-order dynamic model (developed in [23]) was used to assess the orbital stability of a closed-loop system utilizing the enhanced and original orientation-based control strategies, discussed in further detail in Section III. This model consists of four states: elevation angle (θ), azimuth angle (λ), elevation

rate ($\dot{\theta}$), and azimuth rate ($\dot{\lambda}$) (illustrated in Fig. 1). The model is described as follows:

$$\dot{\vec{x}}(t) = \frac{d}{dt} \begin{bmatrix} \theta \\ \lambda \\ \dot{\theta} \\ \dot{\lambda} \end{bmatrix} = \begin{bmatrix} \dot{\theta} \\ \dot{\lambda} \\ \frac{F_\theta(\phi_{cmd})}{mL_t \cos(\lambda)} \\ \frac{F_\lambda(\phi_{cmd})}{mL_t} \end{bmatrix} \quad (1)$$

where m is the kite mass, L_t is the tether length, ϕ_{cmd} is the commanded roll angle, and F_θ and F_λ are the net forces in the elevation and azimuth directions, respectively, as described in [23].

This model treats the desired roll angle as an input to the plant, thereby eliminating the need for low-level roll control by assuming perfect and instantaneous roll tracking. Furthermore, this model assumes that the kite always travels in the direction of its heading, negating the need for closed-loop yaw control. While this model lacks the fidelity of the medium-fidelity dynamic model, it has been used previously in the airborne-wind community in several works ([24], [25], [26]) to analyze both the performance and stability characteristics of kite systems. Its utility in performing these analyses is justified by numerous demonstrations—both simulation-based and experimental—of successful roll angle tracking and very limited sideslip. The state variables used in this model and their respective symbols are listed in Nomenclature.

B. Medium-Fidelity Dynamic Model

In addition to the low-order dynamic model, a medium-fidelity dynamic model was used to simulate the performance of a large-scale kite under the three control strategies discussed in this work. This model was previously experimentally validated in [18].

In this dynamic model, a combination of rigid lifting bodies, each subject to forces and moments induced by lift, drag, buoyancy, and gravity, along with a lumped-mass tether, is used to describe the system. Methods from [27] were utilized to formulate the dynamics of the system while allowing for the inclusion of added mass terms. Ultimately, this model contains 12 state variables (three linear velocities, three angular velocities, three translational positions, and three Euler angles) for the 6-degree-of-freedom kite, in addition to six state variables for each node in the tether (three positions and three velocities). The control inputs are the aileron, elevator, and rudder deflections (denoted by δ_a , δ_e , and δ_r , respectively).

The kite is described by three body-fixed orthonormal unit vectors, \vec{x}_k , \vec{y}_k , and \vec{z}_k , whose origin lies at the intersection of the leading edge of the kite wing and the vertical plane of symmetry, as depicted in Fig. 1. Note that, while the low-order model discussed in Section II-A assumes the x -axis of the kite's body frame points out of the nose of the kite, the medium-fidelity dynamic model described in this section and depicted in Fig. 1 assumes that the kite's x -axis points out of the tail of the kite. This is done for consistency with past work in [14], [19], and [21]. Orthonormal unit vectors \vec{x}_o , \vec{y}_o , and \vec{z}_o are used to describe the inertial reference frame. The state variables describing the position and orientation (and

rates of change of the position and orientation) of the kite evolve according to the nonlinear equations of motion

$$\dot{\vec{v}}_r = M_k^{-1} \left(\vec{r}(\vec{v}_r, [\delta_a, \delta_e, \delta_r]^T) - \vec{C}(\vec{v}_r) \vec{v}_r \right) \quad (2)$$

where

$$\vec{v}_r = \begin{bmatrix} u_{\text{kite}} \\ v_{\text{kite}} \\ w_{\text{kite}} \\ p \\ q \\ r \end{bmatrix} \quad (3)$$

and where u_{kite} , v_{kite} , and w_{kite} are the \vec{x}_k , \vec{y}_k , and \vec{z}_k direction velocities of the kite, respectively, and p , q , and r are the angular velocity components about the \vec{x}_k , \vec{y}_k , and \vec{z}_k axes, respectively. In (2), \vec{v}_r is the relative velocity vector of the kite, the vector $\vec{r}(\vec{v}_r, [\delta_a, \delta_e, \delta_r]^T)$ is composed of the forces and moments acting on the kite, the vector $\vec{C}(\vec{v}_r)\vec{v}_r$ characterizes Coriolis terms, and M_k is an inertial matrix that accounts for added mass. The derivation of these terms can be found in [27]. Readers are referred to [15] and [28] for a detailed derivation of the forces and moments on the kite.

The tether is modeled as a chain of cylindrical links, which are characterized as noncompressive spring-damper elements, connected by nodes. Each node has three translational degrees of freedom and is subject to forces due to tension, drag, and gravity. The mathematical derivation of these forces is available in [29]. The state variables used in this model, along with their respective symbols, are listed in Nomenclature, noting that the roll, pitch, and yaw angles represent standard Euler angles describing the relative orientation of the ground and kite frames.¹

III. CONTROL DESIGN

A. Existing Control Architectures

Control strategies for guiding the flight path of a kite system primarily focus on either tracking periodic roll and yaw setpoints (resulting in figure-eight flight [19], [24]) or tracking a prescribed 3-D path ([23], [30]). Typically, trajectories are modeled as sinusoids using four parameters: roll amplitude (A_ϕ), yaw amplitude (A_ψ), frequency (ω), and the phase offset between the roll and yaw setpoints (p) as

$$\phi_{\text{des}}(t) = A_\phi \sin(\omega t + p) \quad (4)$$

$$\psi_{\text{des}}(t) = A_\psi \sin \omega t \quad (5)$$

where ϕ_{des} is the roll setpoint, ψ_{des} is the yaw setpoint, and t is the time. These trajectories are tracked using proportional-integral-derivative (PID) controllers, which receive the roll and yaw errors (e_ϕ and e_ψ) as inputs and output desired roll and yaw moments ($C_{L,\text{cmd}}$ and $C_{N,\text{cmd}}$). These desired moments are then converted into the aileron and rudder deflections expected to generate these moments (δ_a and δ_r) through a control allocation matrix that considers the effect of each control input on the two moments, which is a function of the apparent velocity of incident flow (v_{app})

¹The medium-fidelity dynamic model used in this work is publicly accessible at <https://github.com/corelab-umich/DoEOceanKiteProject>

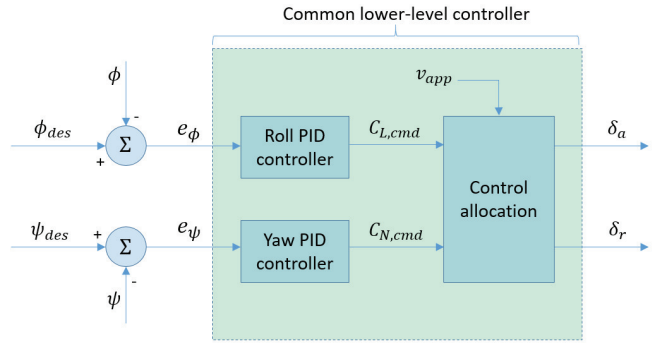


Fig. 2. Block diagram demonstrating an orientation-based controller.

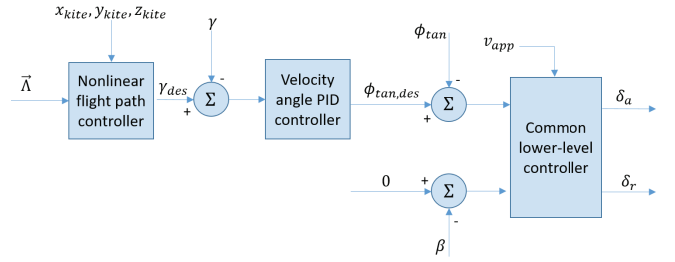


Fig. 3. Block diagram demonstrating a hierarchical path-following controller.

[18]. A block diagram describing this control technique is shown in Fig. 2. Crucially, the mean elevation angle a kite operating in orientation-based control is driven to is not an easily calculable function of the roll and yaw setpoints. In fact, this is difficult to identify without direct experimentation or high-fidelity simulation, yet the elevation angle has a significant impact on kite performance.

The latter of the two common control techniques, path-following control, utilizes a four-layer hierarchical controller (as depicted in Fig. 3) to guide the kite into tracking a prescribed 3-D path [31]. The setpoints that define a figure-eight flight path, given by the vector $\vec{\Lambda}$, include the path center elevation angle (θ_{ctr}), path center azimuth angle (λ_{ctr}), elevation sweep (θ_{sweep}), azimuth sweep (ϕ_{sweep}), and tether length (L_t). The first level selects a desired velocity angle (γ_{des}), which specifies the direction of the kite's velocity vector. The second level selects a desired tangent roll angle ($\phi_{\tan,\text{des}}$), which represents the kite's bank angle relative to the instantaneous sphere it is flying on (whose radius is dictated by the tether length), as needed to achieve the desired velocity angle. The third and fourth layers are comprised of the common lower-level controller shown in Fig. 2, taking in tangent roll error and the hydrodynamic sideslip angle (β) in place of the roll and yaw errors, to compute the aileron and rudder deflections needed to track the path. This control technique has been demonstrated to be extremely effective when applied to airborne kites in practice ([7], [32]) and underwater kites in simulation ([30], [33]). However, simulation-based analysis on underwater kite systems does not consider the practical limitations of measuring each of the variables required for the implementation of the path-following controller, nor does it account for the complexity of tuning this controller in the field.

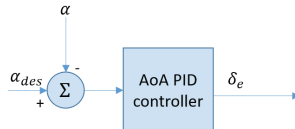


Fig. 4. Block diagram demonstrating the common angle of an attack controller.

All flight controllers discussed in this work use a common controller to modulate the kite's angle of attack (AoA or α) to a desired value (α_{des}) by varying the elevator deflection (δ_e) as shown in Fig. 4. This controller is not included in the above block diagrams, as linearization-based analysis has shown the lateral and longitudinal dynamics to be decoupled under small perturbations [31].

B. Challenges Associated With Path-Following Control

One of the largest challenges of implementing path-following control on an underwater kite lies in obtaining a fast, reliable, and accurate measurement of the kite's position. Despite disturbances induced by ocean waves and swells, a measurement of a kite's z position can be obtained using only an onboard depth sensor. Conversely, measurements of an underwater kite's x and y positions are much more difficult to capture. Existing sensors capable of such measurements, namely USBL systems, suffer from a host of issues. First, these systems are subject to significant measurement noise when moving at the considerable speeds associated with cross-current flight. Furthermore, in typical use cases, USBL systems are complemented by a Doppler Velocity Log (DVL) sensor capable of measuring ground frame velocity by acoustically pinging the seabed. Using these sensors in tandem, a dead reckoned position estimate (via a DVL) is corrected via periodic fixes (via the USBL). With many autonomous underwater vehicles, hours or days can go by between USBL-based fixes, and the DVL-based estimate can accumulate several meters of drift error over this period without serious consequences. While this approach works well in the context of typical autonomous underwater vehicles, such an arrangement is much more problematic for kites, which require positional accuracy typically well within 1 m to execute reliable path-following. Beyond the low quality of measurements made by these systems, USBL units are very costly, driving up the leveled cost of energy (LCOE) of any kite system utilizing one. Lastly, USBL systems emit powerful acoustic signals that can endanger undersea wildlife, thereby limiting the regions where a kite utilizing a USBL can be installed.

Path-following control architectures, like the one displayed in Fig. 3, rely upon hierarchical controllers requiring several layers of sequential control. That being said, in kite systems, a hierarchical control architecture is generally preferred to a centralized control architecture since the use of multiple nested feedback loops provides a necessary level of robustness in the presence of modeling uncertainties. While still preferred to centralized control architectures, the use of multilayered hierarchical control in kite systems presents two primary issues: computational demands and tuning concerns.

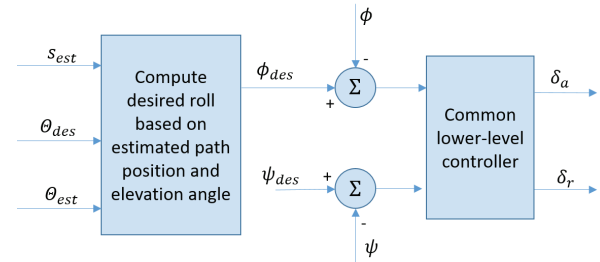


Fig. 5. Block diagram demonstrating the enhanced orientation-based controller.

With regard to computational demands, hierarchical controllers require faster base sampling rates than centralized controllers, as a fundamental assumption of hierarchical control is that the lower levels of control act quickly relative to the upper levels. Additionally, when implementing a hierarchical path-following controller, careful and tedious tuning of all layers of the hierarchical controller is needed to ensure robustness across a range of operational conditions. This tuning process is iterative, requiring the lower level of control to be tuned first before moving up layer by layer, re-tuning each layer at every iteration as needed until the desired stability and tracking objectives are met.

C. Novel Control Technique: Enhanced Orientation-Based Control

The primary contribution of this work is the presentation of a novel control strategy, termed enhanced orientation-based control, which enables a kite to fly in periodic orbits at a desired elevation angle using only orientation measurements and depth measurements. This technique combines the simplicity of orientation-based control with the performance of path-following control. A block diagram describing this control technique is shown in Fig. 5. In this block diagram, S_{est} is the estimated position of the kite on the figure-eight flight path (parameterized between 0 and 2π). An open-loop estimate of $S_{est,OL}$ is calculated as follows using the setpoint frequency (ω):

$$S_{est,OL} = \omega t \bmod 2\pi. \quad (6)$$

While this open-loop estimate of path position was used throughout this work and shown to be sufficient for controlling the kite to a desired elevation angle (as examined in Sections V and VI), a closed-loop estimator can also be implemented if a measurement of azimuth angle is available. Using a (potentially noisy and/or infrequently updated) measurement of the azimuth angle, a Kalman filter can be implemented to calculate a filtered closed-loop estimate (λ_{est}), as follows:

$$\lambda_{est} = \frac{A}{2} \cos S_{est,OL} + K(\lambda_{mes} - \lambda_{est}) \quad (7)$$

where A is the amplitude of the azimuth sweep, K is the corrector gain, and λ_{mes} is the measured azimuth angle. Using this estimate of azimuth, a closed-loop estimate of path position, $S_{est,CL}$, can be obtained as follows:

$$S_{est,CL} = \arcsin \frac{\lambda_{est}}{A/2}. \quad (8)$$

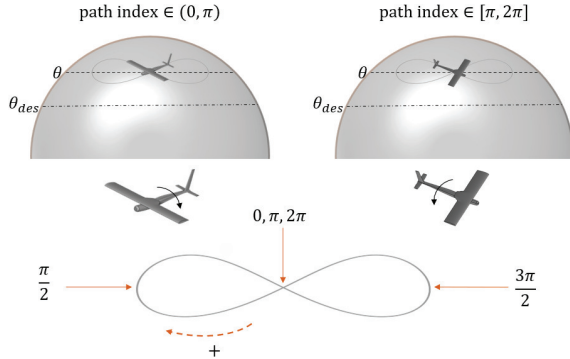


Fig. 6. Diagram showing the roll setpoint augmentation term's sign-changing logic. In the image on the left, the kite is driven to a lower elevation angle by increasing its roll angle positively to target a lower elevation angle θ_{des} . Conversely, in the image on the right, a lower elevation angle is achieved by increasing the kite roll angle in the negative direction.

The estimated elevation angle error shown in this block diagram, θ_{est} , is calculated as follows:

$$\theta_{est} = \arcsin \frac{z_{kite}}{L_t} \quad (9)$$

where z_{kite} is the z -position of the kite (obtained through a depth measurement sensor) and L_t is the deployed tether length. While the yaw angle setpoint trajectory is calculated identically to that of the orientation-based controller, (5), the roll angle setpoint, ϕ_{des} , is calculated as

$$\phi_{des} = A_\phi \sin(\omega t + p) + \cos(S_{est}) c_\theta \quad (10)$$

where c_θ , the output of the elevation angle controller, is the output of the following proportional-integral (PI) controller:

$$c_\theta = k_{p,\theta} e_\theta + k_{i,\theta} \int_0^t e_\theta d\bar{t}. \quad (11)$$

Here, $k_{p,\theta}$ and $k_{i,\theta}$ are proportional and integral gains, respectively, and e_θ is a filtered elevation angle error, which is the output of the following first-order filter:

$$\dot{e}_\theta = \frac{1}{\tau} (e_{\theta,inst} - e_\theta) \quad (12)$$

where $e_{\theta,inst}$ is the instantaneous elevation angle error (given by $\theta_{des} - \theta_{est}$) and τ is the filter constant. The output of the elevation angle controller, c_θ , is modified continuously.

The fundamental premise of the enhanced orientation-based controller is that a desired elevation angle can be reached by appropriately modifying the kite's roll angle based on its estimated position along the figure-eight path. An intuitive illustration depicting the underlying physics that makes this approach work is given in Fig. 6. When presented with a negative elevation angle error, the kite will roll more aggressively on the straightaways of the figure-eight to reduce the elevation angle. Because the sign of the roll adjustment needed to lower the kite's mean elevation angle reverses the sign every half-period based on which direction the kite is flying, the cosine of the estimated path position is multiplied by the output of the elevation angle controller. The result of this added control input is a phase shift in the roll setpoint and an adjustment in magnitude. However, unlike a trial-and-error

TABLE I
NUMBER OF TUNABLE GAINS AND PARAMETERS IN EACH CONTROL ARCHITECTURE

Control Strategy	Tunable Gains and Parameters
Orientation	12
Enhanced Orientation	16
Path-Following	24

process of tuning the phase shift and amplitude to reach a desired elevation angle, the proposed controller performs this adjustment automatically as a function of the elevation angle error, with very little added complexity in terms of required tuning parameters or sensors.

To quantitatively compare the complexity of the three control strategies, the number of control gains and parameters associated with each strategy is shown in Table I. As can be seen in Table I, the path-following control strategy contains twice the number of tunable gains and parameters when compared to the orientation-based strategy and 50% more gains and parameters than the enhanced orientation-based strategy, representing a notable difference in complexity.

IV. ORBITAL STABILITY ANALYSIS

In this section, we analyze the limit cycle stability of the closed-loop system governed by the enhanced orientation-based control strategy. In the context of a kite system, orbital stability means that—under constant environmental conditions and controller parameters—the closed-loop system will converge to a steady limit cycle. Furthermore, when perturbed from this limit cycle, the transient deviations from the nominal trajectory must remain close in magnitude to the magnitude of the perturbation before converging back to the nominal trajectory. In this work, orbital stability is assessed using a Floquet analysis on the low-order dynamic model. This model is used for this analysis for two key reasons. First, elevation angle—the measurement that the enhanced orientation-based controller closes the loop on by adjusting the periodic roll setpoint—is a state in this model (as opposed to a nonlinear function of state variables as in the case of the medium-fidelity model). Furthermore, this dynamic model negates the fast dynamics associated with roll control, instead treating kite roll angle as an input to the plant. Through prior experimental results in [18] and [19], these low-level controllers have been shown to converge quickly and track accurately, demonstrating the fast dynamics associated with roll tracking and validating this assumption. In addition to reducing the number of state variables, making the Floquet analysis feasible to perform, this assumption allows the stability characteristics of the controller to be analyzed directly without considering the effects on downstream controllers used to control the kite to a desired roll angle.

A kite model previously examined in [14] was used to characterize the orbital stability of the closed-loop system under the proposed controller. The plant parameters of this kite model are described in Table II. A more detailed description of the plant model, including the lift-drag characterization of

TABLE II
OPEN-SOURCE KITE PLANT PARAMETERS

Variable	Description	Value	Units
s	Wingspan	10	m
c	Root Chord Length	1	m
AR	Aspect Ratio	11.1	-
TR	Taper Ratio	0.8	-
AP	Airfoil Profile	2412	NACA
n_{turb}	Number of Turbines	4	-
m	Kite Mass	2857	kg
d	Tether Diameter	1.44	cm
$c_{d,\text{thr}}$	Tether Drag Coefficient	0.5	-

TABLE III
LOW-ORDER MODEL OPEN-SOURCE KITE CONTROL PARAMETERS

Variable	Description	Value	Units
L_t	Tether Length	300	m
A_ϕ	Roll Amplitude	40	°
α	Kite AoA	2.5	°
ω	Roll Frequency	0.0349	$\frac{\text{rad}}{\text{s}}$
θ_{des}	Elevation Angle Setpoint	45	°
$k_{p,\theta}$	Elevation Angle Proportional Gain	-3	$\frac{\text{rad}}{\text{rad}}$
$k_{i,\theta}$	Elevation Angle Integral Gain	-0.002	$\frac{\text{rad}}{\text{s}^{-1}}$
T	Figure-eight Period	180	s

each lifting surface, can be found in [14]. Parameters of the controller used in this section are listed in Table III.

A. Defining Orbital Stability

The steady figure-eight flight pattern of the kite can be characterized as a limit cycle. For that limit cycle to be stable, the transient deviations from the nominal trajectory must remain close in magnitude to the perturbation before converging back to the nominal trajectory. In the context of kite systems, in particular, this notion of orbital stability is crucial in ensuring the reliable and safe operation of the system. Floquet analysis can be used to assess this orbital stability.

As mentioned previously, the low-order dynamic model (described in Section II) was used in this analysis. We consider the case of a constant flow speed, allowing the system to be modeled as an autonomous system. For a given set of design, control, and environmental parameters $\vec{P} = \vec{P}_0$, the closed-loop system can be described by

$$\dot{\vec{x}} = f(\vec{x}, \vec{P}) \quad (13)$$

where \vec{x} is the state vector.

To assess orbital stability, we consider a fixed point \vec{x}_0 on the kite's limit cycle trajectory, which resides in the lower-dimensional subspace and represents the point where the nominal trajectory intersects the subspace. To formalize the notion of orbital stability, we define t_k as the k th intersection point of the periodic orbit with the lower-dimensional subspace. This intersection marks the conclusion of the k th period. To be considered orbitally stable, the system must satisfy the

condition that, for every $\epsilon > 0$, there exists some $\delta > 0$ such that

$$\|\vec{x}(t_0) - \vec{x}_0\| < \delta \implies \|\vec{x}(t_k) - \vec{x}_0\| < \epsilon \quad (14)$$

for all positive integer values of k .

Furthermore, the system is classified as orbitally asymptotically stable around \vec{x}_0 if, in addition to meeting the condition defined in (14), the following attractiveness condition is met:

$$\lim_{k \rightarrow \infty} \vec{x}(t_k) = \vec{x}_0. \quad (15)$$

B. Floquet Analysis Formulation

For this analysis, we consider an autonomous system, as described in (13), that admits a steady periodic solution, $\vec{X}_0(t)$, with period T . The realized trajectory can be decomposed into the sum of the steady periodic solution and a deviation from this solution, $\vec{y}(t)$, termed the "disturbance signal." The disturbance signal is then superimposed on the steady solution as follows:

$$\vec{x}(t) = \vec{X}_0(t) + \vec{y}(t). \quad (16)$$

By assuming that f , as defined in (13), is at least twice continuously differentiable, a Taylor series of (16) about \vec{X}_0 can be expressed as follows:

$$\dot{\vec{y}} = A(\vec{X}_0, \vec{P})\vec{y} + \text{HOT} \quad (17)$$

where $A(\vec{X}_0, \vec{P})$ is the matrix of the first partial derivatives of f with respect to the state vector and HOT represents higher-order terms [34]. In linear-system terms, $A(\vec{X}_0, \vec{P})$ represents the periodic, linearized A matrix of the nonlinear system f . Negating the higher-order terms, (17) can be expressed simply as

$$\dot{\vec{y}} \approx A(\vec{X}_0, \vec{P})\vec{y}. \quad (18)$$

This linear equation has n linearly independent solutions $\vec{y}_i(t)$, where n is the number of state variables and $i = 1, 2, \dots, n$. These solutions can be composed into an $n \times n$ fundamental matrix solution of the form $Y(t) = [\vec{y}_1(t) \vec{y}_2(t), \dots, \vec{y}_n(t)]$. Since the system is periodic (with a known period T), $Y(t+T) = [\vec{y}_1(t+T) \vec{y}_2(t+T), \dots, \vec{y}_n(t+T)]$ is also a fundamental matrix solution. Given that (18) has, at most, n linearly independent solutions, and because $\vec{y}_1(t)$ to $\vec{y}_n(t)$ are linearly independent solutions, the vectors $\vec{y}_i(t+T)$ are comprised of linear combinations of $\vec{y}_i(t)$. As such, for some constant matrix Φ , the following equation holds:

$$Y(t+T) = Y(t)\Phi. \quad (19)$$

The matrix Φ , also known as the *monodromy matrix*, describes the cycle-to-cycle dynamics of the system. The eigenvalues of Φ , also known as the Floquet multipliers of the system, determine the local orbital stability of the limit cycle. In particular, all but one of these eigenvalues must lie within the unit circle (where the final eigenvalue is guaranteed to lie at a location of $\lambda = 1$, reflecting the fact that any perturbation that does nothing other than delaying or advancing the time at which the kite intersects the lower-dimensional subspace will result in every successive intersection being correspondingly delayed or advanced).

In this work, the dynamic model described in Section II-A was used in concert with the orientation-based and enhanced orientation-based strategies to numerically derive the monodromy matrix for several representative operating conditions. To perform this analysis, it is necessary to calculate the matrix $A(\vec{X}_0, \vec{P})$ described in (17) and (18). This is the time-varying, linearized A matrix of the closed-loop, nonlinear kite and controller system. Considering the enhanced orientation-based controller and the dynamic model described in Section II-A, the dynamics of the closed-loop system are as follows:

$$\begin{bmatrix} \dot{\theta} \\ \dot{\lambda} \\ \ddot{\theta} \\ \dot{\lambda} \\ \dot{\bar{e}}_\theta \\ \dot{e}_\theta \end{bmatrix} = \begin{bmatrix} 0 & 0 & 1 & 0 & 0 & 0 \\ 0 & 0 & 0 & 1 & 0 & 0 \\ 0 & 0 & 0 & 0 & 0 & 0 \\ 0 & 0 & 0 & 0 & 0 & 0 \\ 0 & 0 & 0 & 0 & 0 & 1 \\ \frac{1}{\tau} & 0 & 1 & 0 & 0 & -\frac{1}{\tau} \end{bmatrix} \begin{bmatrix} \theta \\ \lambda \\ \dot{\theta} \\ \dot{\lambda} \\ \bar{e}_\theta \\ e_\theta \end{bmatrix} + \begin{bmatrix} 0 \\ 0 \\ \frac{\sec(\lambda)F_\theta(\phi_{des}(t, e_\theta, \bar{e}_\theta))}{mL_t} \\ \frac{F_\lambda(\phi_{des}(t, e_\theta, \bar{e}_\theta))}{mL_t} \\ 0 \\ -\frac{\theta_{des}}{\tau} \end{bmatrix} \quad (20)$$

where ϕ_{des} is described in (10) and $\bar{e}_\theta = \int_0^t e_\theta d\bar{t}$. Linearizing this system analytically about a nominal value of the state vector $\vec{x}_{nom} \in \vec{X}_0$ at time t_{nom} yields

$$\begin{bmatrix} \delta\dot{\theta} \\ \delta\dot{\lambda} \\ \delta\ddot{\theta} \\ \delta\dot{\lambda} \\ \delta\dot{\bar{e}}_\theta \\ \delta\dot{e}_\theta \end{bmatrix} = \begin{bmatrix} 0 & 0 & 1 & 0 & 0 & 0 \\ 0 & 0 & 0 & 1 & 0 & 0 \\ 0 & \frac{\partial\ddot{\theta}}{\partial\lambda} & 0 & 0 & \frac{\partial\ddot{\theta}}{\partial\bar{e}_\theta} & \frac{\partial\ddot{\theta}}{\partial e_\theta} \\ 0 & 0 & 0 & 0 & \frac{\partial\dot{\lambda}}{\partial\bar{e}_\theta} & \frac{\partial\dot{\lambda}}{\partial e_\theta} \\ 0 & 0 & 0 & 0 & 0 & 1 \\ \frac{1}{\tau} & 0 & 1 & 0 & 0 & -\frac{1}{\tau} \end{bmatrix} \begin{bmatrix} \delta\theta \\ \delta\lambda \\ \delta\dot{\theta} \\ \delta\dot{\lambda} \\ \delta\bar{e}_\theta \\ \delta e_\theta \end{bmatrix} \quad (21)$$

where

$$\frac{\partial\ddot{\theta}}{\partial\lambda} = \frac{\sec(\lambda)\tan(\lambda)F_\theta(\phi_{des}(t, e_\theta, \bar{e}_\theta))}{mL_t} \quad (22)$$

$$\frac{\partial\ddot{\theta}}{\partial\bar{e}_\theta} = \frac{\sec(\lambda)\partial F_\theta(\phi_{des}(t, e_\theta, \bar{e}_\theta))}{mL_t} \quad (23)$$

$$\frac{\partial\ddot{\theta}}{\partial e_\theta} = \frac{\sec(\lambda)\partial F_\theta(\phi_{des}(t, e_\theta, \bar{e}_\theta))}{mL_t} \quad (24)$$

$$\frac{\partial\dot{\lambda}}{\partial\bar{e}_\theta} = \frac{1}{mL_t} \frac{\partial F_\lambda(\phi_{des}(t, e_\theta, \bar{e}_\theta))}{\partial e_\theta} \quad (25)$$

and

$$\frac{\partial\dot{\lambda}}{\partial e_\theta} = \frac{1}{mL_t} \frac{\partial F_\lambda(\phi_{des}(t, e_\theta, \bar{e}_\theta))}{\partial e_\theta}. \quad (26)$$

The matrix shown in (21) is the symbolic representation of the matrix $A(\vec{X}_0, \vec{P})$ evaluated at a single point along the periodic orbit \vec{X}_0 . Given the complex, expressions used to describe the partial derivatives of $\dot{\theta}$ and $\dot{\lambda}$ with respect to λ , \bar{e}_θ , and e_θ , it was impractical to derive a fully symbolic representation of $A(\vec{X}_0, \vec{P})$ in terms of all of the system parameters and corresponding partial derivative expressions evaluated along the nominal trajectory. As such, this matrix was identified numerically using MATLAB/Simulink. For a given kite model,

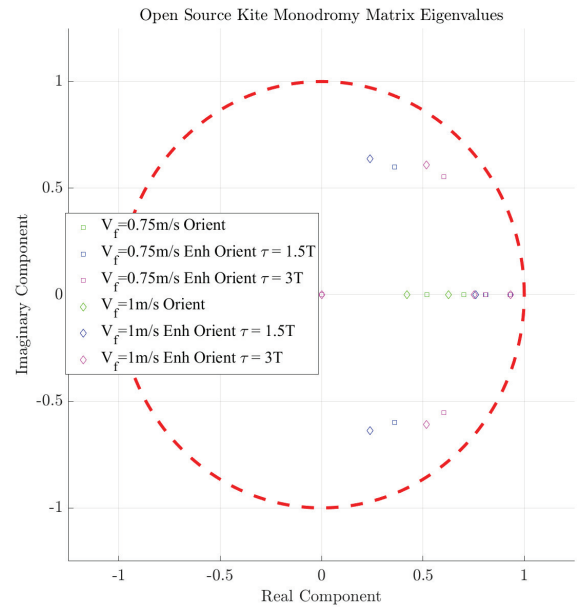


Fig. 7. Eigenvalues of the monodromy matrix under the enhanced and original orientation-based control for the open-source kite model under multiple flow conditions and elevation angle filter time constants.

control strategy, and set of operating conditions, the dynamics of the kite were simulated in MATLAB/Simulink using the nonlinear model shown in (20), until a consistent periodic orbit was achieved. From there, the time-varying matrix $A(\vec{X}_0, \vec{P})$ was identified by linearizing the system about its periodic orbit via numerical perturbation using MATLAB's *linearize* function. Using this time-varying matrix, the monodromy matrix was then identified for a given set of parameters via numeric integration.

C. Floquet Analysis Results

Following the procedure outlined above, the eigenvalues of the monodromy matrix (i.e., the Floquet multipliers) were identified for two environmental conditions as well as three control strategies—original (nonenhanced) orientation-based control, enhanced orientation-based control with an elevation angle filter constant of $1.5T$, and enhanced orientation-based control with an elevation angle filter constant of $3T$, where T is the figure-eight period. Note that the orbital stability of the path-following control strategy was not examined, as it was demonstrated previously in [21] using a distinct dynamic model of similar order.

Utilizing the model parameters given in Table III, the nonunity Floquet multipliers for the three control strategies and the two environmental conditions are shown in Fig. 7. The same analysis was performed for both the open-source and proprietary model under two undisclosed environmental conditions representative of the proprietary kite's intended operating conditions. The calculated Floquet multipliers for the same three control strategies are shown in Figs. 8 and 9. In all cases, all Floquet multipliers are shown to be within the unit circle, thereby demonstrating orbital stability.

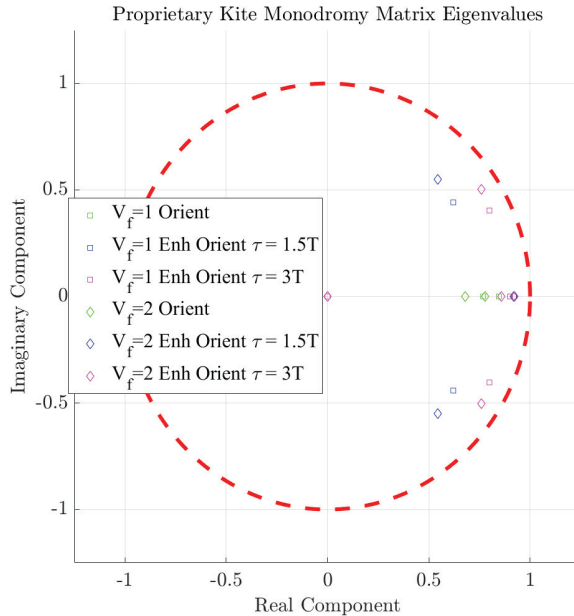


Fig. 8. Eigenvalues of the monodromy matrix under enhanced and original orientation-based control for the proprietary kite model under multiple flow conditions and elevation angle filter time constants.

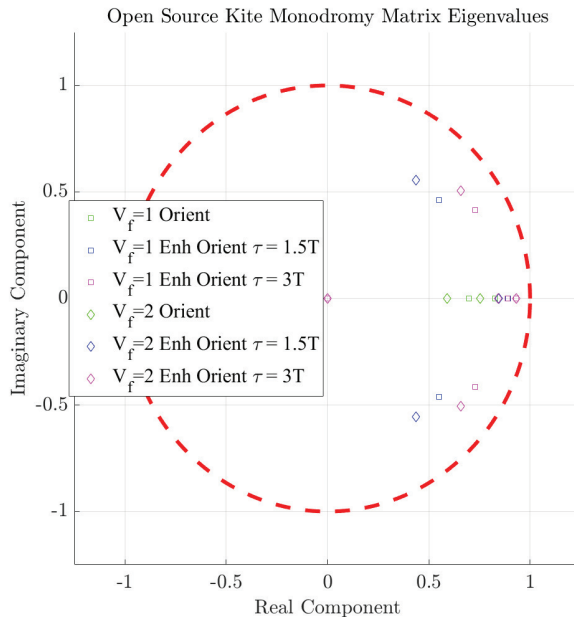


Fig. 9. Eigenvalues of the monodromy matrix under the enhanced and original orientation-based control for the open-source kite model under identical environmental conditions to the proprietary kite.

V. SIMULATION STUDY

In this section, simulations using the medium-fidelity dynamic model are presented to benchmark the performance of the enhanced orientation-based control strategy, as well as the original orientation-based control strategy, to a well-tuned path-following controller. In the simulation studies discussed in this section, a full-scale model applicable to both considered kite designs was utilized. Note that the simulation results presented in this section for the proprietary kite are normalized

TABLE IV
OPEN-SOURCE KITE CONTROL PARAMETERS

Variable	Description	Value	Units
L_t	Tether Length	500	m
a	Path Width	90	m
b	Path Height	30	m
α_{set}	Kite AoA Setpoint	8	°
θ_{des}	Elevation Angle Setpoint	30	°
$k_{p,\theta}$	Elevation Angle Proportional Gain	-3	$\frac{\text{rad}}{\text{rad}}$
$k_{i,\theta}$	Elevation Angle Integral Gain	-0.01	$\frac{\text{s}^{-1}}{\text{s}^{-1}}$

by the following expression:

$$P_{\text{norm}} = \frac{\frac{P}{v_f^3}}{\frac{P_{\text{avg,max}}}{v_f^3}} \quad (27)$$

where P is the power, P_{norm} is the normalized power, and $P_{\text{avg,max}}$ and v_f^3 correspond to the lap-averaged power and flow conditions that result in the largest value of (P/v_f^3) across all flow conditions, respectively.

A. Performance Comparison: Path-Following, Orientation-Based, and Enhanced Orientation-Based Control

The performance of the three control strategies was assessed at three flow speeds with a consistent tether length. Path parameters for the path-following controller were defined based on guidelines defined in [14]. The orientation-based controller was tuned to track sine-wave approximations of the roll-and-yaw angles achieved by the path-following controller. The enhanced orientation-based controller utilized the same yaw setpoint trajectory but augmented the roll trajectory as described in Section III, driving the kite to the same mean elevation angle achieved by the path-following controller. Across the three control strategies, a common controller was utilized to control the kite's angle of attack to a constant value.

The control parameters used for the open-source kite in this simulation are listed in Table IV. The three flow speeds assessed in these simulations ranged from 0.5 to 1 m/s.

Using the open-source kite model under the described control and environmental conditions, the raw and normalized lap-averaged power outputs for the three strategies are shown in Figs. 10 and 11.

Simultaneously, using the proprietary kite model, the normalized, lap-averaged power outputs for the three strategies are shown in Fig. 12 for three nondimensionalized flow speeds and a constant tether length and elevation angle setpoint.

As shown in Figs. 10 and 12, the enhanced orientation-based control strategy generated between 88.4% and 97.3% of the power generated by the path-following controller for the open-source kite and between 81.1% and 86.5% of the power generated by the path-following controller for the proprietary kite. At the same time, orientation-based control alone generated a mere 48.9%–53.6% of the power generated by the full path-following controller for the open-source kite and between 68.7% and 69.9% of the power generated by the full path-following controller for the proprietary kite. To

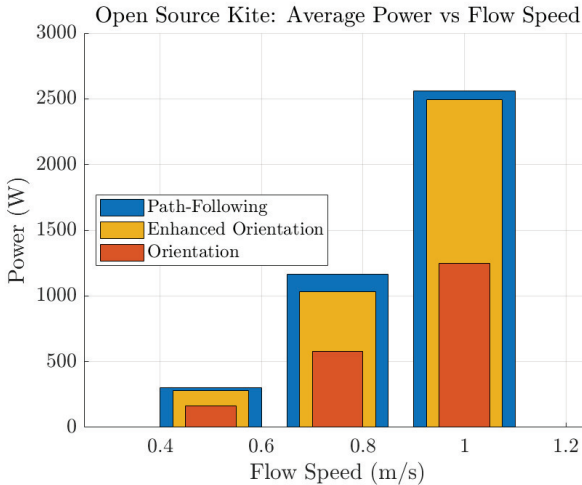


Fig. 10. Average power versus flow speed for path-following, enhanced orientation-based, and original orientation-based control strategies, for the open-source kite design.

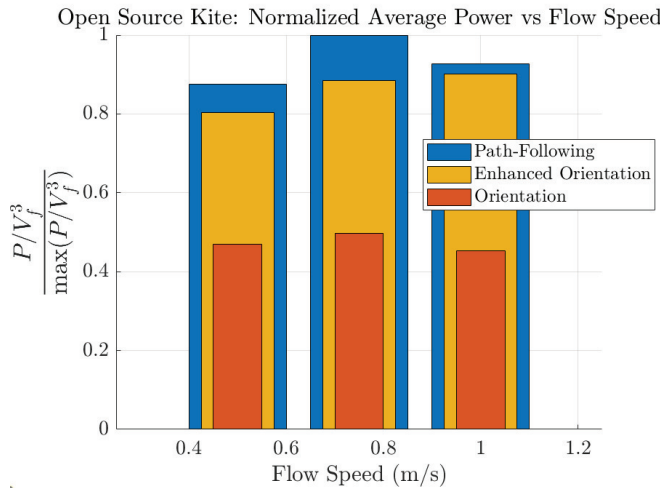


Fig. 11. Normalized average power versus flow speed for path-following, enhanced orientation-based, and original orientation-based control strategies, for the open-source kite design.

date, this is the first direct performance comparison between kite systems using an orientation-based and path-following controller.

For both kites, the enhanced orientation-based control strategy is shown to perform comparably to the path-following controller. For the open-source kite design, the raw and normalized power profiles for the three control strategies at a flow speed of 0.75 m/s are shown in Figs. 13 and 14. Normalized power profiles under the three control strategies using the proprietary kite with an arbitrary flow profile are shown in Fig. 15.

Traces of the final flight paths achieved by the three control strategies are shown for the open-source kite design in Fig. 16 and for the proprietary kite design (normalized to the tether length) in Fig. 17. While the kite's elevation angle was driven by the same mean elevation angle as the path-following controller, the path flown by the enhanced orientation-based controller is comparatively oblong, with lower elevation

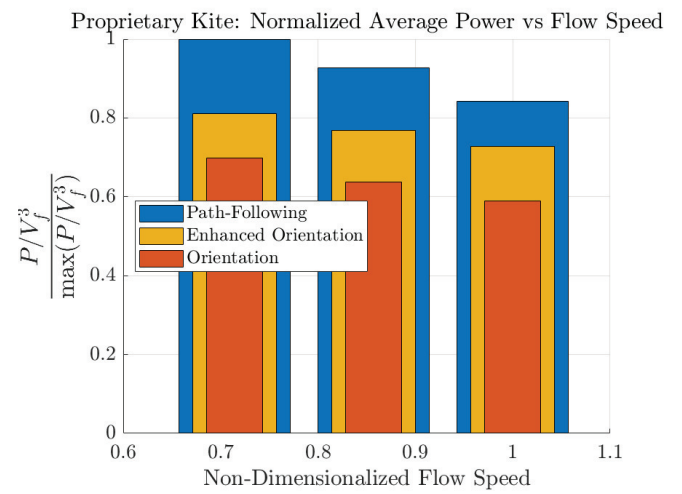


Fig. 12. Normalized power versus flow speed for path-following, enhanced orientation-based, and original orientation-based control strategies, for the proprietary kite design.

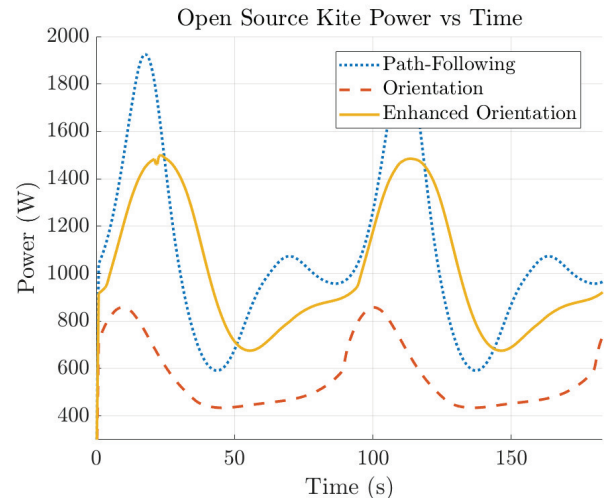


Fig. 13. Power profile for the open-source kite design utilizing the three control strategies operating in a 0.75-m/s flow.

angles at the edges of the figure-eight than at the center. This suboptimal path shape leads the enhanced orientation-based controller to perform marginally worse than the path-following controller when a well-selected path geometry is flown. However, the benefit of the enhanced orientation-based controller lies in its significantly lower complexity.

VI. EXPERIMENTAL VALIDATION

In this section, the experimental validation of the enhanced orientation-based control strategy will be presented and benchmarked against the original orientation-based approach using a scaled-down prototype of the proprietary kite discussed previously. To validate the proposed control strategy, a prototype kite of unspecified scale was tested experimentally in a large lake with over 30 m of available depth and negligible current over the entire test domain. Note that details regarding the kite's size and precise testing location cannot be disclosed due

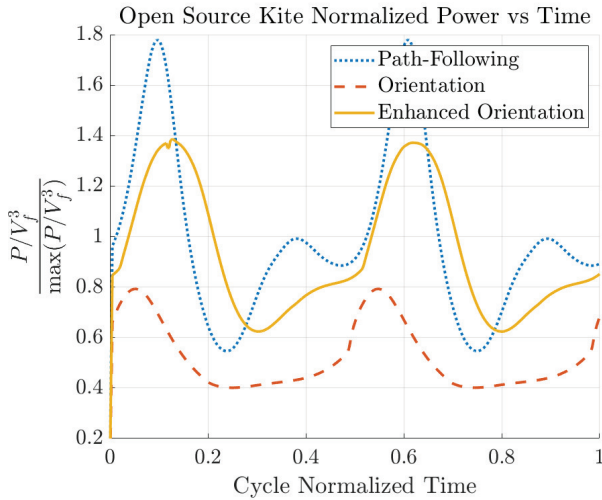


Fig. 14. Normalized power profile for the open-source kite design utilizing the three control strategies operating in a 0.75-m/s flow.

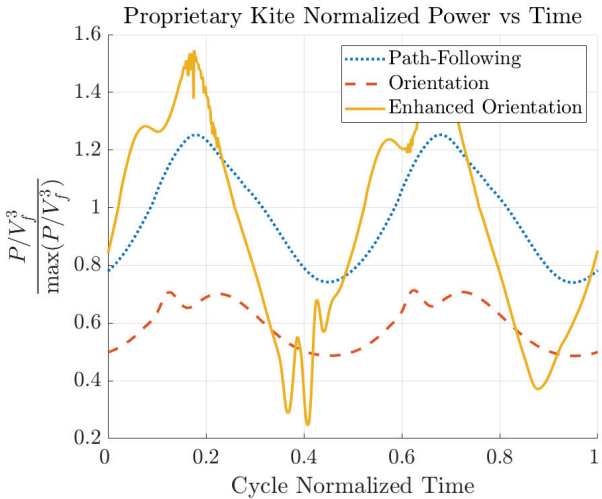


Fig. 15. Power profile for the proprietary kite utilizing the three control strategies operating in a realistic flow environment.

to the proprietary nature of the project. In these experiments, the kite was towed behind a boat at a constant speed to simulate an ocean current. A diagram depicting the experimental setup is shown in Fig. 18.

For these experiments, the integral gain in the enhanced orientation-based controller ($k_{i,\theta}$) was set to zero, as proportional control was found to be sufficient to drive the kite sufficiently close to the desired elevation angle. Additionally, as in the simulated case, the enhanced and original orientation-based controllers tracked the same yaw setpoint trajectories, with the roll setpoint trajectory modified as a function of elevation angle error as described in Section III.

The average normalized powers generated by the kite in these experiments across a range of flow speeds and tether lengths are shown in Fig. 19. Power generation under enhanced orientation-based control consistently exceeded power generation under the original orientation-based control. Time-series

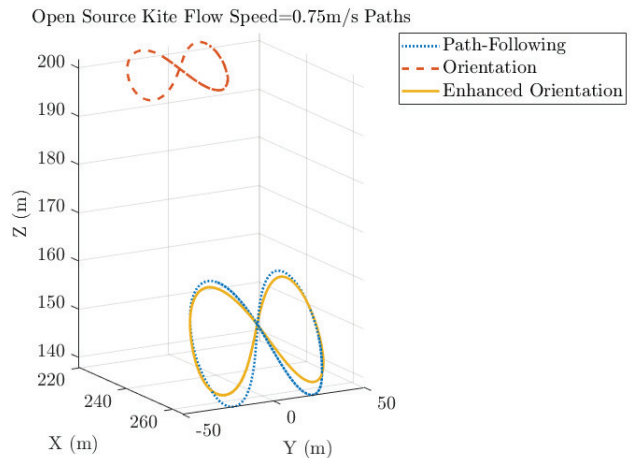


Fig. 16. Flight trajectories flew by the open-source kite for a flow speed of 0.75 m/s. As shown, the enhanced orientation-based controller drives the kite to a comparable elevation angle as the path-following controller despite an initial offset.

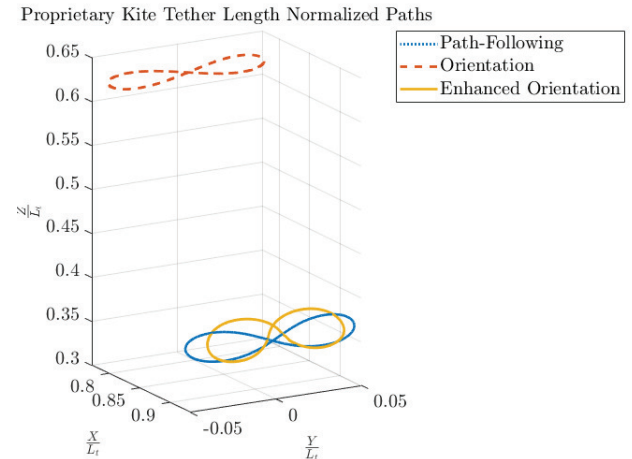


Fig. 17. Flight trajectories flew by the proprietary kite for an arbitrary flow profile. The enhanced orientation-based controller is shown to drive the kite to a comparable elevation angle as the path-following controller despite an initial offset.

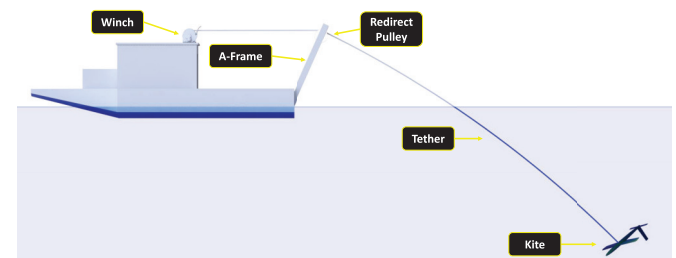


Fig. 18. Diagram depicting the experimental setup including the kite, tether, A-frame (used to suspend the redirect pulley), redirect pulley, and winch (used to adjust tether length).

comparisons of normalized power data for a single flow condition and tether length are plotted in Fig. 20. This figure also shows the predicted power generated using the medium-fidelity simulation model. While the simulation pre-

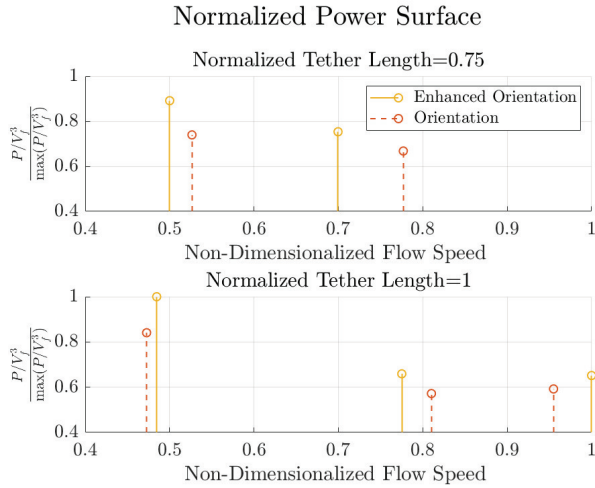


Fig. 19. Experimentally obtained normalized power generated by the enhanced orientation-based and original orientation-based control strategies.

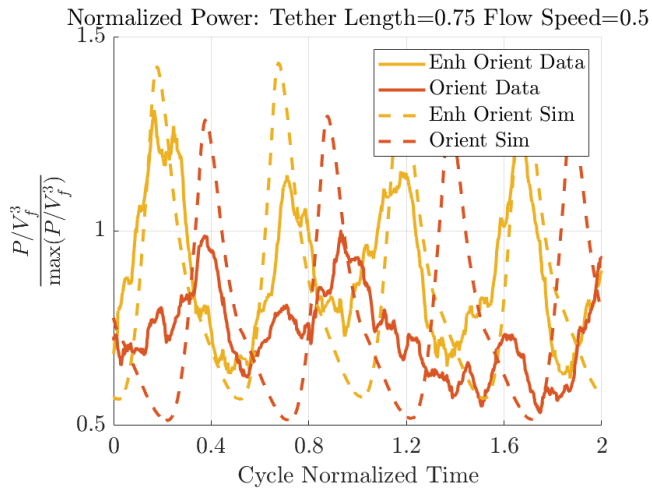


Fig. 20. Experimentally obtained normalized time-series data comparing power generated under enhanced and original orientation-based control under similar tether length and flow conditions along with simulation-based predictions.

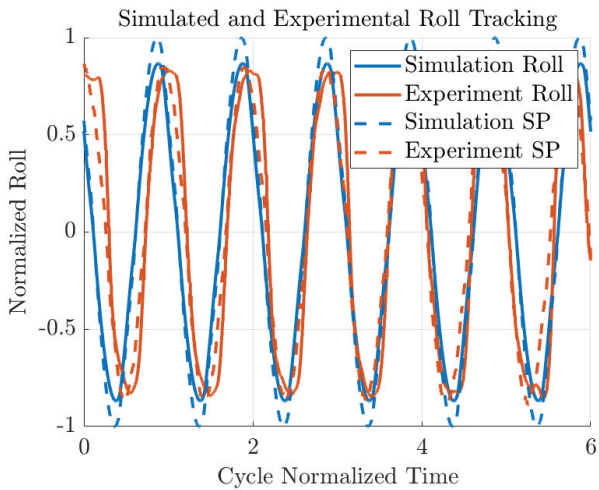


Fig. 21. Normalized experimental and simulation-predicted roll and roll setpoints.

dictions generally agree with the data, the simulation was conducted under the assumption of a constant flow speed

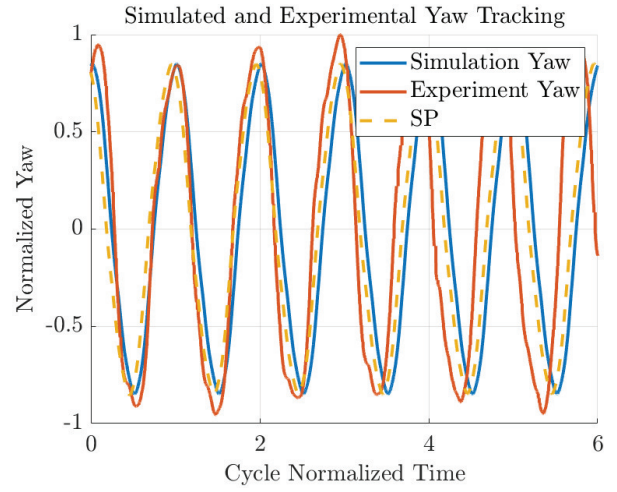


Fig. 22. Normalized experimental and simulation-predicted yaw tracking.

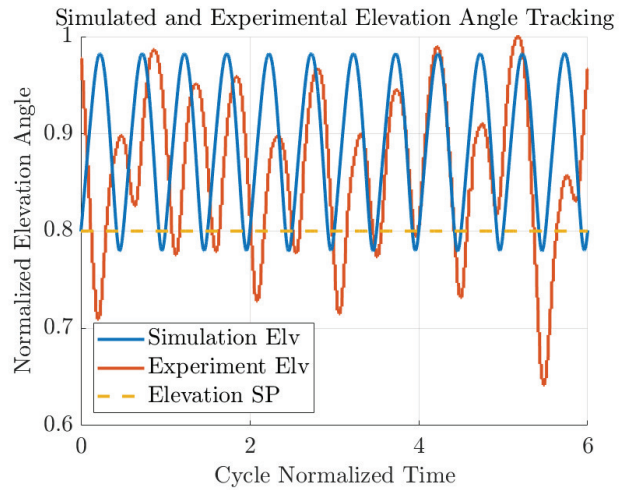


Fig. 23. Normalized experimental and simulation-predicted roll elevation angle and setpoint.

(equal to the root mean square average speed of the boat), whereas the actual boat exhibited some speed variation due to time-varying loading from the tether. Additional figures comparing the roll tracking, yaw tracking, and elevation angle tracking for this flow condition and tether length, along with the simulated predictions of these values, are shown in Figs. 21–23, respectively. In all cases, the measurements and setpoints are normalized by the largest value of the associated variable. Note that in Fig. 23, the measured elevation angle is shown to vary significantly between cycles, leading to imperfect elevation-angle tracking. This was largely caused by a combination of the boat's heave and nonconstant velocity.

As shown in Fig. 19, the enhanced orientation-based control strategy outperformed the original orientation-based control strategy by 9.6%–18.8%, demonstrating a sizable increase in power generation. Note that the tow speeds across test cases vary slightly between comparable data points, as the speed of the boat over the ground was not perfectly constant. Furthermore, the root-mean-cubed flow speed over a given trial was used to represent the average flow speed over the

trial, given that power generated is proportional to flow speed cubed [10].

While significant, the enhancement in performance is shown to be more limited at high tow speeds. This can be attributed to size limitations on the available space for figure-eight flight. In particular, the higher kite speeds that are made possible through enhanced orientation-based control result in larger figure-eight paths (for a given period) at lower elevation angles. Because the kite is operating in a towed setup, with the tether release point slightly above the surface of the water, it is operating at a relatively shallow depth. As a consequence, sufficiently large figure-eight paths at sufficiently low elevation angles will cause the kite to breach the surface. The only way to avoid this is to curtail flight by intentionally either: 1) increasing the elevation angle setpoint or 2) decreasing the figure-eight period (or both). It is at high tow speeds where this curtailment was required (since the kite was pushing the limits of what could be achieved with the tow testing system at these tow speeds), and more curtailment was required for the enhanced orientation-based controller.

VII. CONCLUSION

In this work, a novel kite control strategy, termed enhanced orientation-based control, was presented. In this control modality, a kite is driven to a desired elevation angle through modification of a periodic roll trajectory. The new control strategy was shown to drive a kite to converge to a stable limit cycle through the presented Floquet analysis. Simulations show the enhanced orientation-based controller to generate between 88.4% and 97.3% of the power generated by the path-following controller for one kite model and between 81.1% and 86.5% of the power generated by the path-following controller for another kite model, all without requiring the need for expensive and often unreliable localization sensors. This demonstrates a sizable improvement compared to the original orientation-based control strategy, which generated between 48.9% and 53.6% of the power generated by the path-following controller for one kite model and between 68.7% and 69.9% of the power generated by a path-following control strategy for another kite model. Lastly, the novel control strategy was tested experimentally in a lake-based tow testing setup. The enhanced orientation-based control strategy was shown in experiments to consistently outperform the orientation-based control strategy by between 9.6% and 18.8%. The novel control strategy proposed and tested in this work offers high performance without the need for expensive and often unreliable underwater localization sensors and difficult-to-tune multi-tiered hierarchical controllers, driving down the LCOE and improving the economic viability of these renewable energy systems.

REFERENCES

- [1] K. A. Haas, H. M. Fritz, S. P. French, B. T. Smith, and V. Neary, "Assessment of energy production potential from tidal streams in the United States," Georgia Tech Res. Corp., Atlanta, GA, USA, Tech. Rep. OSTI 1219367, 2011.
- [2] K. A. Haas, H. M. Fritz, S. P. French, and V. Neary, "Assessment of energy production potential from ocean currents along the United States coastline," Georgia Tech Res. Corp., Atlanta, GA, USA, Tech. Rep. DOE/EE/2661-10, 2013.
- [3] ARPA-E SHARKS. Accessed: Apr. 2, 2023. [Online]. Available: <https://arpa-e.energy.gov/?q=arpa-e-programs/sharks>
- [4] A. LiVecchi et al., "Powering the blue economy: Exploring opportunities for marine renewable energy in maritime markets," U.S. Dept. Energy, Washington, DC, USA, Tech. Rep. DOE/GO-1020195157, 2019.
- [5] X. Zeng and R. He, "Gulf stream variability and a triggering mechanism of its large meander in the south Atlantic bight," *J. Geophys. Res., Oceans*, vol. 121, no. 11, pp. 8021–8038, Nov. 2016.
- [6] C. L. Archer and K. Caldeira, "Atlas of high altitude wind power," Dept. Global Ecol., Carnegie Inst. Sci., Stanford, CA, USA, Tech. Rep. 2008, vol. 260. [Online]. Available: <http://www.mdpi.com/1996-1073/2/2/307/s1>
- [7] Windlift.(2019). *Windlift Website*. [Online]. Available: <https://www.windlift.com>
- [8] Kitepower.(2022). *Kitepower Website*. [Online]. Available: <https://thekitepower.com>
- [9] Minesto.(2019). *Minesto Website*. [Online]. Available: <https://www.minesto.com>
- [10] M. Loyd, "Crosswind kite power," *J. Energy*, vol. 4, no. 3, pp. 106–111, 1980.
- [11] P. Williams, B. Lansdorp, and W. Ockels, "Optimal crosswind towing and power generation with tethered kites," *J. Guid., Control, Dyn.*, vol. 31, no. 1, pp. 81–93, Jan. 2008.
- [12] B. Houska and M. Diehl, "Optimal control of towing kites," in *Proc. 45th IEEE Conf. Decis. Control*, Dec. 2006, pp. 2693–2697.
- [13] L. T. Paiva and F. A. C. C. Fontes, "Optimal control of underwater kite power systems," in *Proc. Int. Conf. Energy Sustainability Small Developing Economies (ES2DE)*, Jul. 2017, pp. 1–6.
- [14] A. Abney, J. Fine, and C. Vermillion, "Drag-mitigating dynamic flight path design and sensitivity analysis for an ultra-long tether underwater kite," *J. Dyn. Syst., Meas., Control*, vol. 147, no. 1, Jan. 2025, Art. no. 011001, doi: [10.1115/1.4064379](https://doi.org/10.1115/1.4064379).
- [15] J. Daniels, J. Reed, M. Cobb, A. Siddiqui, and C. Vermillion, "Optimal cyclic spooling control for kite-based energy systems," *IFAC-PapersOnLine*, vol. 53, no. 2, pp. 12719–12725, 2020. [Online]. Available: <https://www.sciencedirect.com/science/article/pii/S2405896320324976>
- [16] J. Reed, J. Daniels, A. Siddiqui, M. Cobb, M. Muglia, and C. Vermillion, "Optimal cyclic control of an ocean kite system in a spatiotemporally varying flow environment," in *Proc. Amer. Control Conf. (ACC)*, May 2021, pp. 596–601.
- [17] G. Licita, S. Sieberling, S. Engelen, P. Williams, R. Ruiterkamp, and M. Diehl, "Optimal control for minimizing power consumption during holding patterns for airborne wind energy pumping system," in *Proc. Eur. Control Conf. (ECC)*, Jun. 2016, pp. 1574–1579.
- [18] A. Abney et al., "Autonomous closed-loop experimental characterization and dynamic model validation of a scaled underwater kite," *J. Dyn. Syst., Meas., Control*, vol. 144, no. 7, Jul. 2022, Art. no. 071005, doi: [10.1115/1.4054141](https://doi.org/10.1115/1.4054141).
- [19] J. Reed et al., "Experimental validation of an iterative learning-based flight trajectory optimizer for an underwater kite," *IEEE Trans. Control Syst. Technol.*, vol. 32, no. 4, pp. 1240–1253, Jul. 2024.
- [20] J. B. Fine, J. Reed, K. Naik, and C. Vermillion, "Predictive control of a morphing energy-harvesting kite," in *Proc. IEEE Conf. Control Technol. Appl. (CCTA)*, Aug. 2022, pp. 1246–1252.
- [21] J. Reed, A. Abney, K. D. Mishra, K. Naik, E. Perkins, and C. Vermillion, "Stability and performance of an undersea kite operating in a turbulent flow field," *IEEE Trans. Control Syst. Technol.*, vol. 31, no. 4, pp. 1663–1678, Jul. 2023.
- [22] J. B. Fine, C. M. McGuire, J. Reed, M. Bryant, and C. Vermillion, "Optimal cyclic control of a structurally constrained span-morphing underwater kite in a spatiotemporally varying flow," in *Proc. Amer. Control Conf. (ACC)*, May 2023, pp. 2084–2090.
- [23] G. B. Silva, L. T. Paiva, and F. A. C. C. Fontes, "A path-following guidance method for airborne wind energy systems with large domain of attraction," in *Proc. Amer. Control Conf. (ACC)*, Jul. 2019, pp. 2771–2776.

- [24] M. Denlinger, "Extremum seeking algorithms for optimal periodic control with application to buoyant air turbines," Ph.D. dissertation, 2018. [Online]. Available: <https://www.proquest.com/dissertations-theses/extremum-seeking-algorithms-optimal-periodic/docview/2205094635/se-2>
- [25] F. Trevisi, I. Castro-Fernández, G. Pasquinelli, C. E. D. Riboldi, and A. Croce, "Flight trajectory optimization of fly-gen airborne wind energy systems through a harmonic balance method," *Wind Energy Sci.*, vol. 7, no. 5, pp. 2039–2058, Oct. 2022.
- [26] M. C. R. M. Fernandes, S. Vinha, L. T. Paiva, and F. A. C. C. Fontes, " L_0 and L_1 guidance and path-following control for airborne wind energy systems," *Energies*, vol. 15, no. 4, p. 1390, Feb. 2022.
- [27] T. I. Fossen, *Handbook of Marine Craft Hydrodynamics and Motion Control*. Hoboken, NJ, USA: Wiley, 2011.
- [28] J. Reed, J. Daniels, A. Siddiqui, M. Cobb, and C. Vermillion, "Optimal exploration and charging for an autonomous underwater vehicle with energy-harvesting kite," in *Proc. Amer. Control Conf. (ACC)*, Jul. 2020, pp. 4134–4139.
- [29] C. Vermillion, T. Grunnagle, R. Lim, and I. Kolmanovsky, "Model-based plant design and hierarchical control of a prototype lighter-than-air wind energy system, with experimental flight test results," *IEEE Trans. Control Syst. Technol.*, vol. 22, no. 2, pp. 531–542, Mar. 2014.
- [30] J. Reed, M. Cobb, J. Daniels, A. Siddiqui, M. Muglia, and C. Vermillion, "Hierarchical control design and performance assessment of an ocean kite in a turbulent flow environment," *IFAC-PapersOnLine*, vol. 53, no. 2, pp. 12726–12732, 2020. [Online]. Available: <https://www.sciencedirect.com/science/article/pii/S2405896320325015>
- [31] S. Rapp, "Robust automatic pumping cycle operation of airborne wind energy systems," Ph.D. dissertation, Dept. Aerosp. Eng., Delft Univ. Technol., Delft, The Netherlands, Mar. 2021.
- [32] Makani.(2019). *Makani Website*. [Online]. Available: <https://makanipower.com>
- [33] M. Cobb et al., "Iterative learning-based path optimization with application to marine hydrokinetic energy systems," *IEEE Trans. Control Syst. Technol.*, vol. 30, no. 2, pp. 639–653, Mar. 2022.
- [34] A. H. Nayfeh and B. Balachandran, *Applied Nonlinear Dynamics*. Hoboken, NJ, USA: Wiley, 1995.